

GSA SUPPLEMENTAL MATERIAL

Rochelle-Bates, N., Roberts, N.M.W., Sharp, I., Freitag, U., Verwer, K., Halton, A., Fiordalisi, E., van Dongen, B.E., Swart, R., Ferreira, C.H., Dixon, R., Schröder, S., 2020, Geochronology of volcanically associated hydrocarbon charge in the Pre-Salt Carbonates of the Namibe Basin, Angola: *Geology* G48019

SUPPLEMENTAL FILE S1: SUPPLEMENTAL INFORMATION

Locality Information

The Chapeu Armado locality (Fig. 1/S1), is a transtensional relay zone associated with a distinct north eastward stepping “jog” in the NW-SE striking basin bounding fault system, which was exploited by paleo-drainage systems. Similar short NE-trending fault jogs are evident in the Bero and Ponte Negra areas, and are interpreted as breaching relay zones or linking faults to the dominant NW-SE (more rift-orthogonal) trending fault array. Closely-spaced NW-SE and NE-SW trending faults and associated fractures are abundant and show dip and oblique slip kinematics.

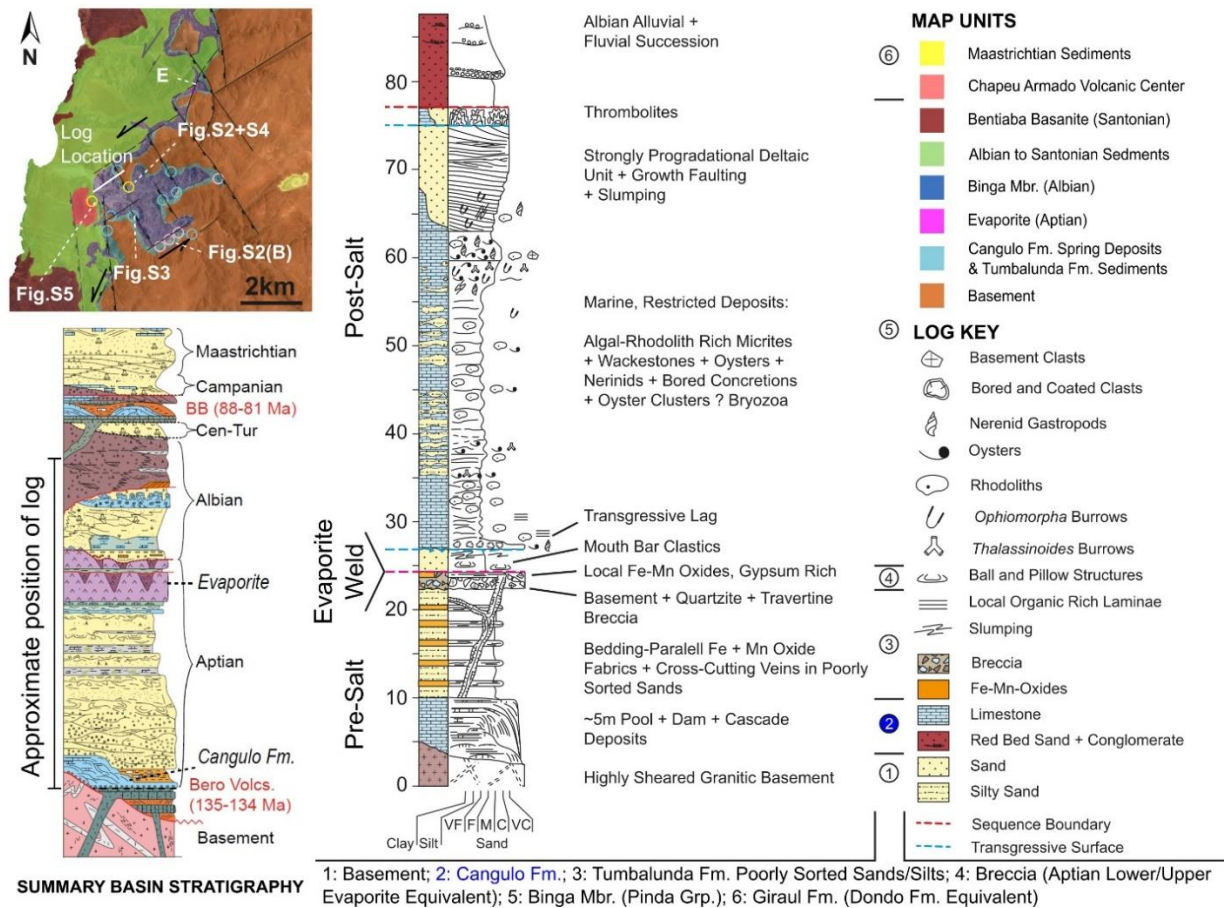


Figure S1, log through Pre- and Post-Salt sedimentary sequence at the mouth of the Chapeu Armado paleovalley. Position of logged interval within the overall basin stratigraphy (from Fig. 1) is indicated on the left. The sampled formation is indicated in blue (Cangulo Fm.). Log location is marked on the locality map (modified from Fig. 1), along with sample localities (circled yellow), Cangulo Fm. spring carbonates (circled light blue), Cangulo Fm. siliceous spring deposits (circled pink) and figure locations. E indicates location with ~40m of preserved evaporite.

The sampled Cangulo Fm. outcrop is c.15 m in height. Within the travertine pool facies, the cream coloured micritic host rock is displaced by stratabound veins, non-stratabound veins up to around 5cm in thickness, and vugs (Fig S2). Fibro-prismatic calcite cement (C_1) is bituminous and contains abundant volatile organic compounds that give them a distinct kerogenic smell when crushed. C_1 vein fills were only identified at Chapeu Armado and at a similar outcrop in the Bero River valley. Siliceous Cangulo Fm. cascades (circled pink, Fig. 1/S1) in the Chapeu Armado region are confined to the edge of the complex along mineralised faults. The faults are associated with thermobaric ladder and “zebra” like hydraulic fracture and cement fills, including barite, iron and silica minerals (Fig. S2B). Similar fabrics were observed in the immediate Pre-Salt at Ponte Negra, Piambo and in the Bero River valley. The Cangulo Fm. carbonate systems interfinger laterally with and are overlain by Pre-Salt alluvial-fluvial clastics of the Tumbalunda Formation, which display bedding-parallel Fe and Mn oxide mineralization at Chapeu Armado.

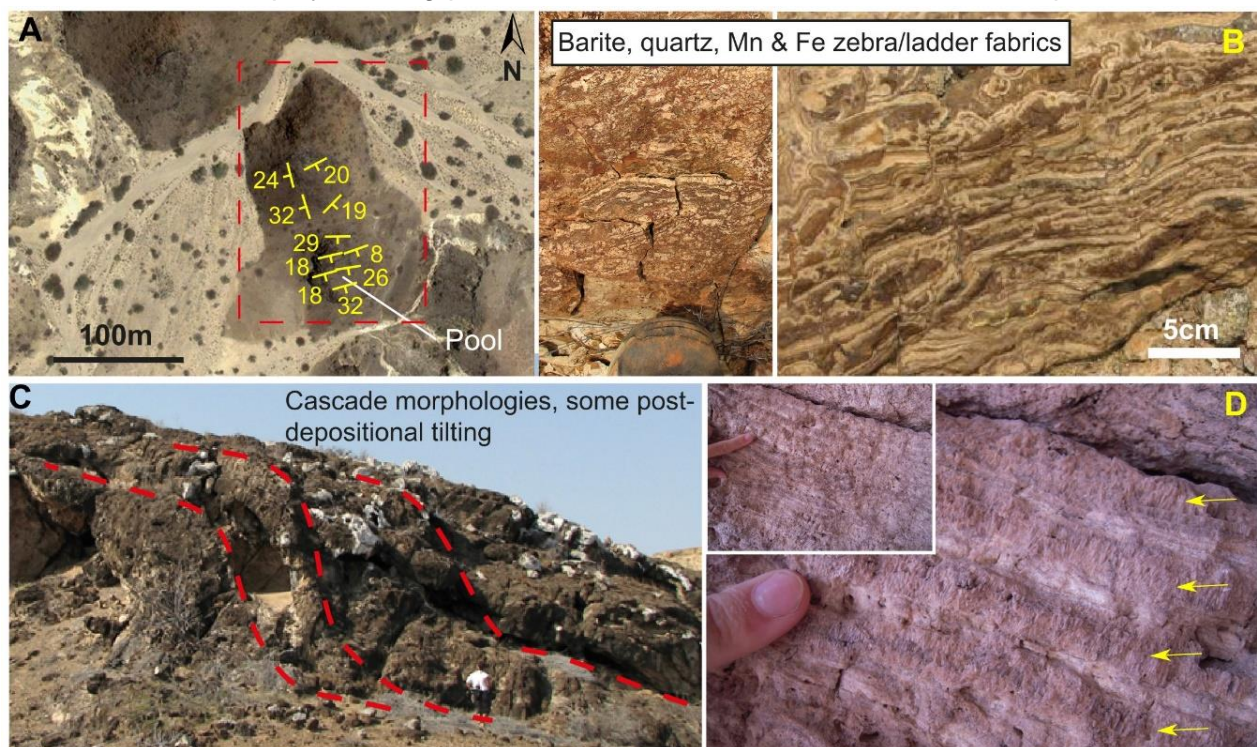


Figure S2, Cangulo Fm. depositional geometries with C_1 veins at the sample locality and overpressure fabrics at a nearby locality. **A**, Google Earth image of C_1 sample outcrop with depositional strike/dip data; depositional geometries are exploited by/subparallel to C_1 veins. **B**, Ladder and zebra type fabrics composed of barite, Mn and Fe minerals associated with siliceous cascades along a nearby fault zone. **C**, Prograding cascades at the sampled outcrop (red dashed lines); figure for scale. **D**, Pale cream micritic host rock (pool facies) with slightly darker and rougher fibrous C_1 veins (yellow arrows) exploiting the slightly (post-depositionally) tilted bedding geometries at the sample outcrop.

Speleothem fabrics are locally common within the Cangulo Fm. (Fig. S4). Locally, the vugs are also filled by well-rounded sandstones, with shell and echinoderm fragments. The sediments are visually identical to those in the overlying marine Binga Mbr. (Pinda Group, Albian; Fig. S3), and are believed to have been deposited in vugs upon evaporite withdrawal. These relationships suggest karstification (and possibly dolomitization) prior to deposition of the Binga Mbr. or prior

to evaporite removal. As such, the speleothems are considered Cretaceous in age. The same relationship is present in the Cangulo region outcrops, where extensive karstification of the Cangulo Fm. carbonates is evident (Baqués et al., 2016).

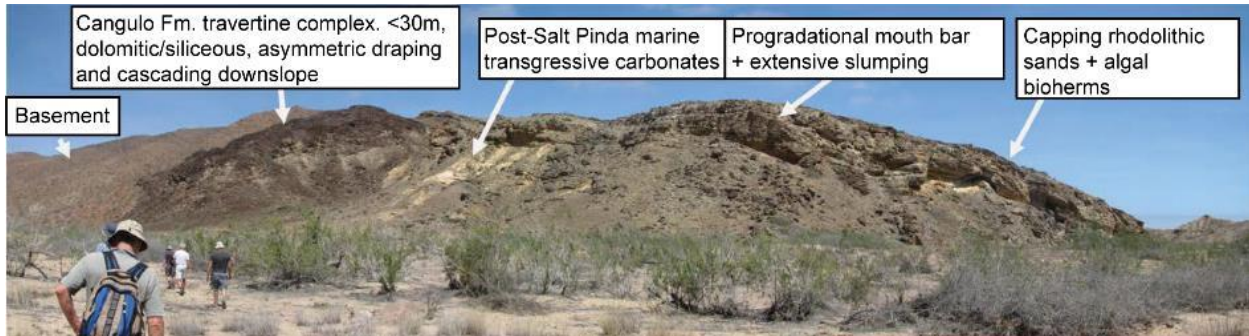


Figure S3, Cangulo Fm. Pre-Salt travertine cascades sitting on basement and overlain by Post Salt Pinda Group (Binga Mbr.) marine sedimentary rocks. The evaporite has been completely removed at this location, resulting in Pinda marine sedimentary rocks grounding directly onto the Pre-Salt.

Eleven kilometers south along the basin bounding fault (at the Cangulo paleovalley), lacustrine Pre-Salt mud/siltstones and marlstones intercalated with the Cangulo Fm. contain high enough total organic carbon (TOC) to be effective source rocks. The best-preserved Cangulo Fm. host-rock from Chapeu Armado (e.g. Fig. S8 (left)) does not appear to be rich enough in organic matter to form an effective source rock. However, it could be that the organic-rich source facies (presumably lacustrine) were not observed at the study locality or are not well-preserved.

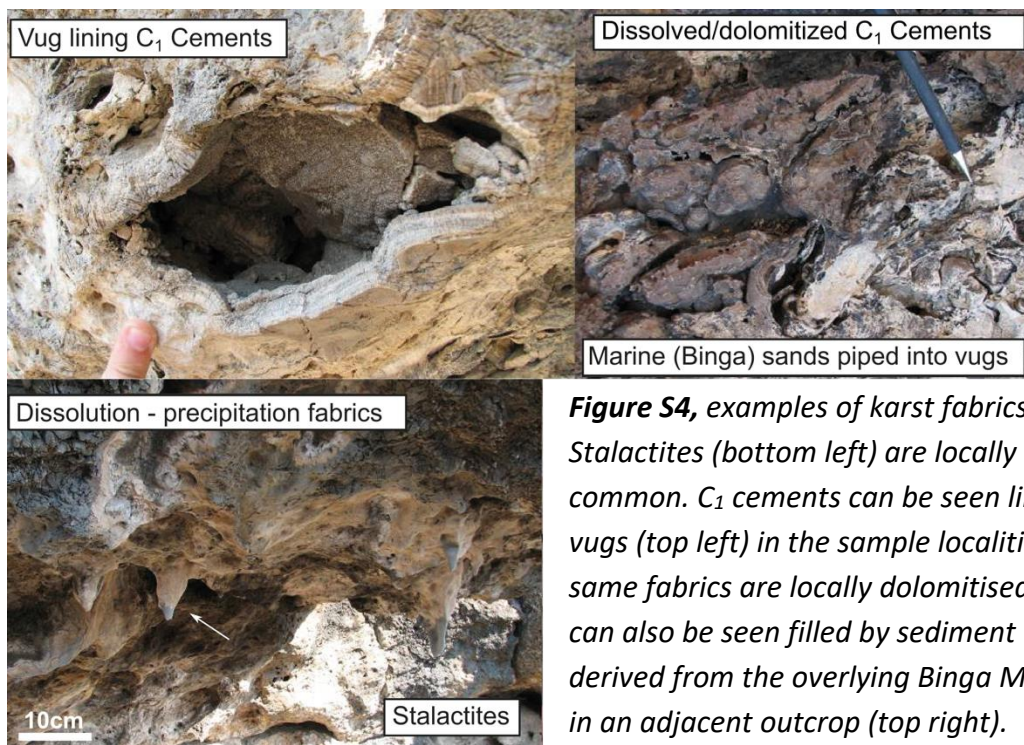


Figure S4, examples of karst fabrics. Stalactites (bottom left) are locally common. C_1 cements can be seen lining vugs (top left) in the sample localities. The same fabrics are locally dolomitised and can also be seen filled by sediment derived from the overlying Binga Member in an adjacent outcrop (top right).

In the Chapeu Armado region, the Aptian-aged evaporites have almost completely been removed by dissolution, and instead are represented by a breccia composed of angular to rounded clasts of basement, travertine and quartzite. Over 4 km laterally this passes into a 40m thick body of evaporitic remnants (Location E, Fig. S1). At the study locality, Post-Salt marine

sandstones/carbonates of the Albian Binga Mbr. (Pinda Group) rest directly on Pre-Salt lithologies (Fig. S3). The Binga Mbr. is a restricted marine, transgressive, organic-rich deposit that is a potential (Post-Salt) source rock. Large vugs filled with bitumen were identified within the Binga Mbr. close to the Chapeu Armado volcanic center, suggesting localized (forced) in-situ maturation of organic matter within this unit as a result of Late Cretaceous volcanism.

A distinctive nephelinite plug and dyke complex immediately west of the main paleovalley gives the Chapeu Armado (“Armoured Hat”) locality its name (Fig. S5). Chapeu Armado is capped by a thick layer of pyroclastic breccia overlain by slightly amygdaloidal nephelinite lava flows with vertical columnar jointing. The variable altitude of the basanite flow across the east face attests to considerable faulting and deformation of the wall-rock stratigraphic sequence. The pyroclastic breccia below the summit lavas is poorly sorted with volcanic, sedimentary and granitic clasts up to 15cm set in a coarse altered gritty matrix. The breccia is several metres thick and its lower contact is obscured by scree. The lavas also enclose many crustal xenoliths. Stratigraphic control on the Chapeu Armado complex is limited. Nephelinite plugs and dykes cross-cut the underlying Post-Salt sedimentary rocks and Bentiaba Basanite, and the main volcanic plug extends above the surrounding Bentiaba Basanite basalts and Maastrichtian marine sedimentary rocks. Nephelinite boulders in nearby Miocene beach deposits, as reported by Beetz, (1934), indicate that the nephelinite complex is pre-Miocene in age.

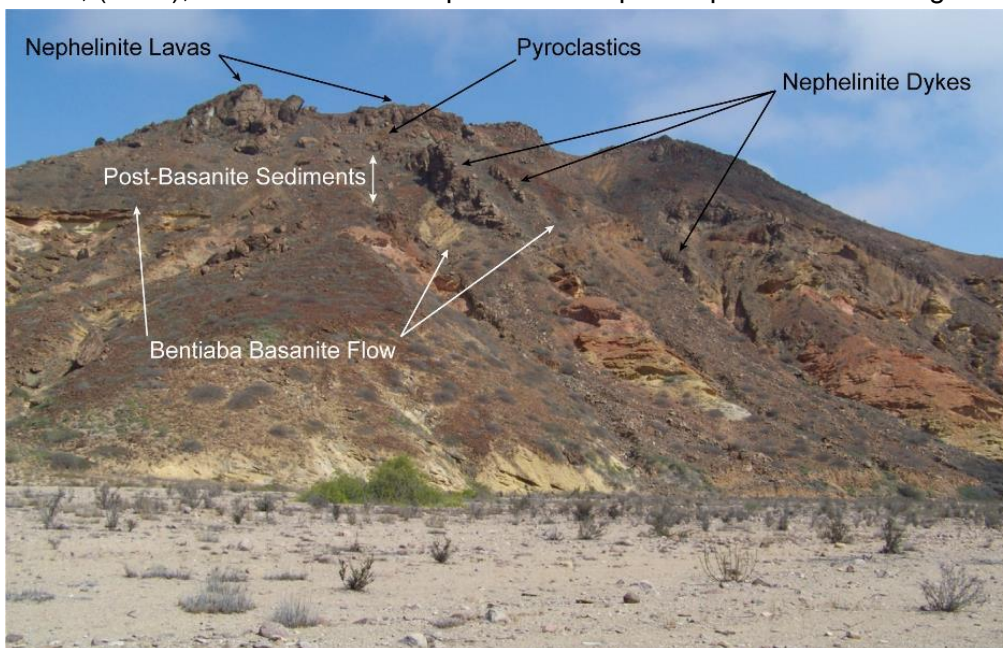


Figure S5,
Eastern Face of the Chapeu Armado igneous complex. Height of exposure is approximately 50m.

Sample Locations

Sample	Analysis	Latitude (DD)	Longitude (DD)
CA-1	$^{40}\text{Ar}/^{39}\text{Ar}$	-14.46123	12.35627
CA-2	$^{40}\text{Ar}/^{39}\text{Ar}$	-14.46023	12.35962
25_3	U-Pb	-14.45680	12.36810
25_5	U-Pb	-14.45680	12.36810
204_1	U-Pb	-14.45725	12.36803
208_1	U-Pb	-14.45709	12.36796
208_2	U-Pb	-14.45709	12.36796
210_1	U-Pb	-14.45702	12.36803

U-Pb Geochronology

U-Pb geochronology via the in-situ Laser Ablation Inductively Coupled Mass Spectrometer (LA-ICP-MS) method was conducted at the Geochronology & Tracers Facility, British Geological Survey (Nottingham, UK). The method utilises a New Wave Research 193UC excimer laser ablation system, coupled to a Nu Instruments Attom single-collector sector-field ICP-MS. The method for calcite (Li et al., 2014; Coogan et al., 2016; Roberts and Walker, 2016; Roberts et al., 2017; Beaudoin et al., 2018) is adapted from that used for zircon (see Spencer et al., 2014), with some modifications. The laser parameters used are 80 – 100 μm static spots, fired at 10 Hz, with a $\sim 7 \text{ J.cm}^{-2}$ fluence, for 20 seconds of ablation. Material is pre-ablated to clean the sample site with a 150 μm spot for 3 seconds. Spot ablations were carried out along growth zones that were identified via binocular microscope and informed by thin sections taken from the same samples. Care was taken to avoid bitumen-inclusion-rich zones, which were clearly visible during sampling. Ablation sites were checked optically after analysis, and irregular ablations due to crystallographic effects or aberrations during ablation were discounted from the dataset. Standard sample bracketing uses NIST 614 glass for normalization of $^{207}\text{Pb}/^{206}\text{Pb}$ ratios (Woodhead and Hergt, 2007) for Pb-Pb ratios, and a carbonate reference material developed in-house for $^{206}\text{Pb}/^{238}\text{U}$ ratios (WC-1; Roberts et al., 2017). Data are reduced using the time-resolved-analysis function in the Nu Attolab software, and an in-house excel spreadsheet. Normalization is based on the measured/accepted ratio derived from the session-based drift-corrected mean of the primary WC-1 reference material. No downhole correction is made – the downhole $^{206}\text{Pb}/^{238}\text{U}$ ratios are flat and linear, and the 20 second ablation signal is not split into shorter integrations. No common lead correction is made; those ages that are deemed robust (based on low MSWD), are determined from lower intercepts on a Tera-Wasserburg plot. All regressions are unanchored as the spread in data permits assessment of the upper intercept accurately. Clear outliers in Tera-Wasserburg plots, i.e. statistical outliers, are rejected from the age regressions, and are likely a consequence of analysing inclusions. Resulting Tera-Wasserburg plots (Fig. 4, Fig. S8) show the Model 1 ages and have uncertainties quoted as age $\pm x/y$, where x is without systematic uncertainties and y is with these propagated (see Horstwood et al., 2016). The reproducibility of the primary WC-1 reference material is around 1 to 1.5% per session. An estimate of the session reproducibility is propagated (as excess variance) onto the sample data. Additional systematic uncertainties include the decay constant uncertainty and the uncertainty on the reference material age of 2.75%. An additional carbonate material, Duff Brown Tank, was measured to provide a control on accuracy and precision. An isotope dilution age of 64.04 \pm 0.67 Ma is provided by Hill et al., (2016). In each session the resulting age of Duff Brown was within uncertainty of this value. The pooled data from all sessions yield an age of 63.6 \pm 1.4 Ma (2σ without systematic uncertainties propagated). Data are presented in Data Repository File DR2.

The method uses a calcite reference material to analyse dolomite in addition to calcite. There may be a small bias in the resulting age due to the use of a different matrix; at present we do not understand how big this bias is, but we expect it to be on the order of a few percent at maximum. This is largely within the uncertainty of the final age data after propagation of systematic

uncertainties. The dolomite age (57 Ma) is 29 Myrs younger than the calcite forming event (86 Ma), i.e. a difference of over 30%. Thus, the potential matrix bias of a few percent is much smaller than the difference between the events we are dating. The same set-up for U-Pb is used for the trace element mapping, except that the Attom is run in linkscan mode (see Roberts et al., 2017).

Line rasters were analysed using 40 x 40 μm squares rastered at 20 $\mu\text{m}/\text{sec}$ with a repetition rate of 10 Hz and fluence of 8 $\text{J}\cdot\text{cm}^{-2}$. Data are normalised to NIST614 silicate glass using ^{44}Ca as an internal standard. A secondary standard was not used, so results are semi-quantitative. Iolite software (Paton et al., 2011) is used to generate the maps from series of line rasters. The position of the map area is presented in Fig. S6 and the maps are shown in Fig. S7.

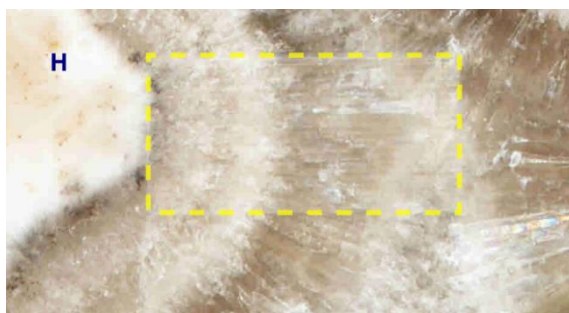


Figure S6, image of polished block surface with botryoidal C_1 growing on host micrite (H). Area of C_1 chosen for elemental mapping indicated by yellow stippled box. The mapped area is 1 x 2 mm.

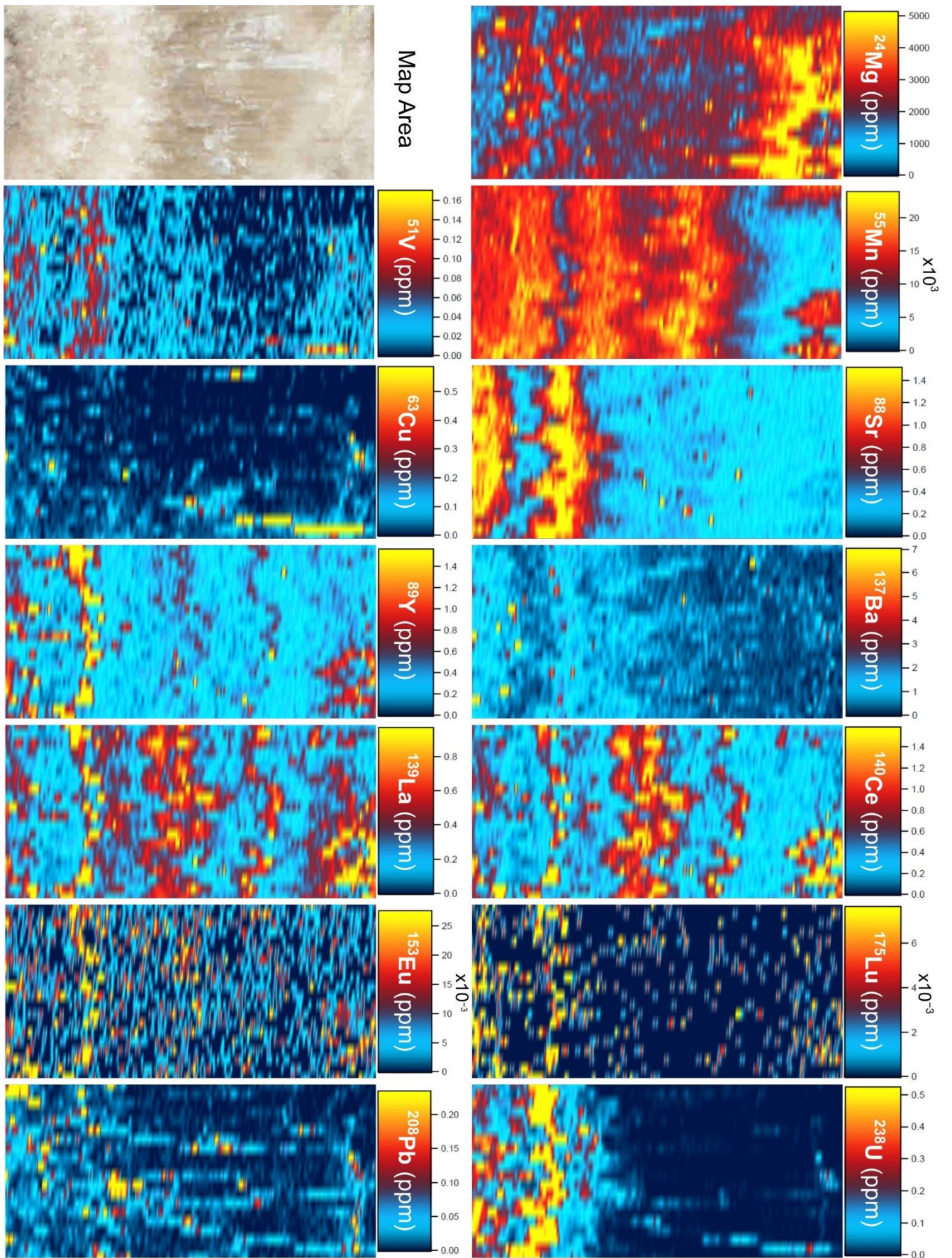
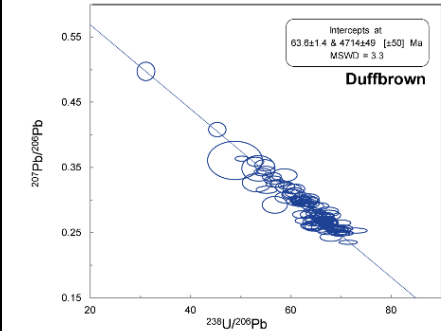


Figure S7, map area and elemental maps for C_1 cement. The mapped area is 1 x 2 mm.

Laboratory & Sample Preparation	
Laboratory name	NERC Isotope Geosciences Laboratory
Sample type/mineral	Calcite, Dolomite
Sample preparation	In-situ in polished block
Imaging	None
Laser Ablation System	
Make, Model & type	ESI/New Wave Research, 193UC
Ablation cell & volume	NWR TV2
Laser wavelength (nm)	193nm
Pulse width (ns)	3-4ns
Fluence (J.cm ⁻²)	~7 J.cm ⁻²
Repetition rate (Hz)	10 Hz
Ablation duration (secs)	30 secs
Ablation pit depth / ablation rate	~40 µm pit depth, measured using an optical microscope
Spot size (µm)	80 or 100µm
Sampling mode / pattern	Static spot ablation
Carrier gas	100% He, Ar make-up gas combined ca. 50% along sample line
Cell carrier gas flow (l/min)	0.6 l/min
ICP-MS Instrument	
Make, Model & type	Nu Instruments Attom SC-SF-ICP-MS
Sample introduction	Free air aspiration of desolvator
RF power (W)	1300W
Make-up gas flow (l/min)	0.8 l/min Ar
Detection system	Discrete dynode MassCom ion counter
Masses measured	202, 204, 206, 207, 208, 232, 238
Integration time per peak	200 µs (202, 204, 208, 232), 400 µs (206), 100 µs (207, 238) 80 sweeps per integration
Total integration time per reading (secs)	0.30 seconds
Sensitivity / Efficiency (% , element)	~0.2 % for Uranium
IC Dead time (ns)	15 ns
Data Processing	
Gas blank	60 second on-peak zero subtracted
Calibration strategy	NIST614 for Pb-Pb, WC-1 for Pb-U
Reference Material info	Primary: WC-1 254 +/- 6 Ma (2s) - Roberts et al., 2017 Secondary: Duff Brown 64.04 +/- 0.67 Ma (2s) - Hill et al., 2016
Data processing package used / Correction for LIEF	Nu Instruments TRA acquisition software, in-house spreadsheet data processing

Mass discrimination	$^{207}\text{Pb}/^{206}\text{Pb}$, $^{206}\text{Pb}/^{238}\text{U}$ normalised to reference materials	
Common-Pb correction, composition and uncertainty	Unanchored (model 1) regressions in Tera-Wasserburg (Semi Total-Pb) plots	
Uncertainty level & propagation	Ages in the data table are quoted at 2s absolute and include systematic uncertainties, propagation is by quadratic addition	
Quality control / Validation		Duff Brown over the course of the analytical sessions gave 63.6 ± 1.4 Ma, MSWD = 3.3 (without propagation of systematic uncertainties)

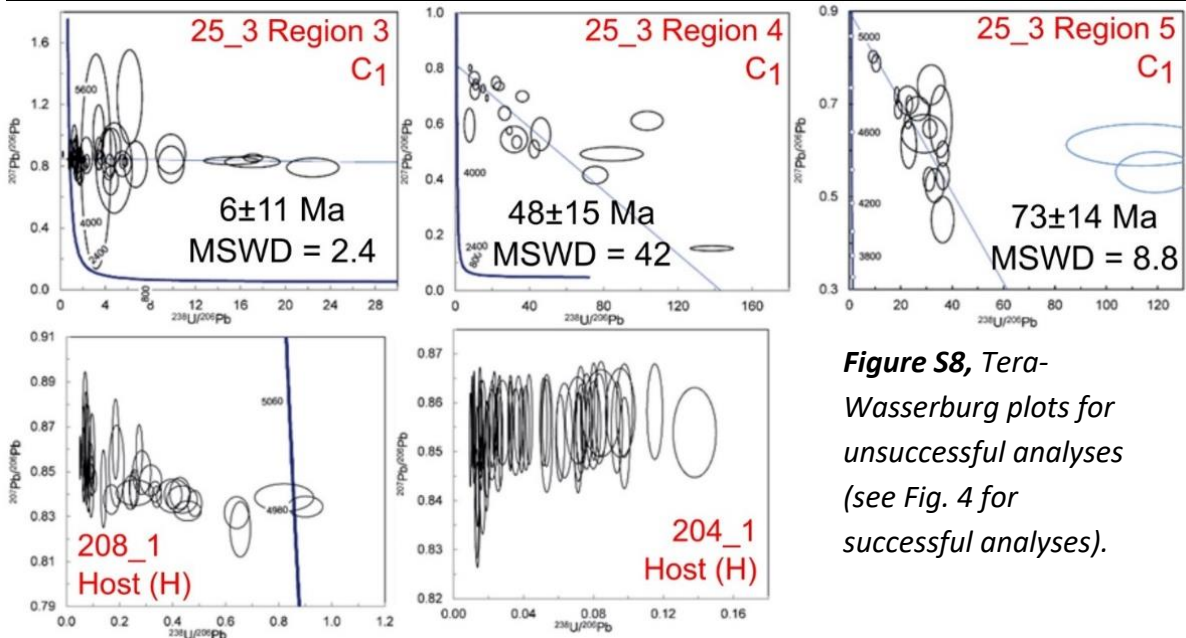


Figure S8, Tera-Wasserburg plots for unsuccessful analyses (see Fig. 4 for successful analyses).

Samples:

Sample	Phases Analyzed	Latitude (DD)	Longitude (DD)	Sample Image (scale bar = 1cm)
25_3	C ₁	-14.45680°	12.36810°	

25_5	C ₁ (rejected)	-14.45680°	12.36810°	
204_1	H (rejected) C ₁ Dol ₂ C ₄ (rejected)	-14.45725°	12.36803°	
208_1	H (rejected)	-14.45709°	12.36796°	
208_2	C ₁	-14.45709°	12.36796°	
210_1	C ₁	-14.45702°	12.36803°	

⁴⁰Ar/³⁹Ar Geochronology

Sample preparation. The samples were crushed using a pestle and mortar and the crushate was sieved and washed repeatedly in de-ionised water to remove dust and clay particles from the surfaces of all the size fractions. Using a binocular microscope, basalt groundmass pieces were picked, selecting pieces free from alteration. The picked separates were cleaned ultrasonically in acetone and de-ionised water, dried using the hot plate, and packaged in aluminium foil packets of ca. 10mm x 10mm in size prior to irradiation.

Irradiation. Samples were irradiated at the McMaster Nuclear Reactor (McMaster University, Canada) for 107 hours. Cadmium shielding was used and the samples were held in position 8D. Neutron flux was monitored using biotite mineral standard GA1550 which has an age of 99.738 ± 0.104 Ma (Renne et al., 2010). Standards were packed for irradiation, either side of the unknown samples and analysed using the single grain fusion method using a 1059nm CSI fibre laser and a MAP215-50 mass spectrometer. The J Values were then calculated by linear extrapolation between the 2 measured J values, the values for each sample are shown in the Data Repository File DR3 and a 1% error on J is used.

Analysis. The irradiated samples were loaded into an ultra-high vacuum system and a 1059nm CSI fibre laser was focussed into the sample chamber and was used to step-heat basalt. After passing through a liquid nitrogen trap, extracted gases were cleaned for 5 minutes using three SAES AP-10 getters, two running at 450°C and one at room temperature, following which the gases were let into a MAP 215-50 mass spectrometer for measurement, the mass discrimination value was measured at 283 for $^{40}\text{Ar}/^{36}\text{Ar}$ (using a calibration noble gas mixture of known composition). System blanks were measured before and after every one or two sample analyses. Gas clean-up and inlet is fully automated, with measurement of ^{40}Ar , ^{39}Ar , ^{38}Ar , ^{37}Ar , and ^{36}Ar , each for ten scans, and the final measurements are extrapolations back to the inlet time.

Data Reduction. The system blanks measured before and after every one or two sample analysis were subtracted from the raw sample data. Results were corrected ^{37}Ar and ^{39}Ar decay, and neutron-induced interference reactions. The following correction factors were used:

$$(^{39}\text{Ar}/^{37}\text{Ar})\text{Ca} = 0.00065 \pm 0.00000325, (1)$$

$$(^{36}\text{Ar}/^{37}\text{Ar})\text{Ca} = 0.000265 \pm 0.000001325, (2)$$

$$(^{40}\text{Ar}/^{39}\text{Ar})\text{K} = 0.0085 \pm 0.0000425, (3)$$

based on analyses of Ca and K salts. Ages were calculated using the atmospheric $^{40}\text{Ar}/^{36}\text{Ar}$ ratio of 298.56 (Lee et al., 2006) and decay constants of Renne et al., (2011). All data corrections were carried out using an Excel macro and ages were calculated using Isoplot 4.15 (Ludwig, 2012). All ages are reported at the 2σ level and include a 1% error on the J value. Plateau criteria of at least 50% of the ^{39}Ar release in at least 3 consecutive steps were used and the probability-of-fit of the weighted mean age to the steps is greater than 5%. $^{40}\text{Ar}/^{39}\text{Ar}$ data are presented in Data Repository File DR3.

Sample CA-1. Step-heating analysis of sample CA-1 produces a plateau age of 89.8 ± 1.8 Ma which contains 64.5 % of the released ^{39}Ar . The inverse isochron calculation using these data gives an age, the same as that from the plateau calculation, of 89.1 ± 3.0 Ma. The $^{40}\text{Ar}/^{36}\text{Ar}$ intercept from this inverse isochron calculation is within error of the atmospheric value (of 298.56, Lee et al., 2006) at 337 ± 86 .

Sample CA-2. The data from step heating of CA-2 do not meet the statistical criteria for a plateau age (outlined in Data Reduction). The inverse isochron calculation gives an age of 86.3

± 3.0 Ma (the same as the pooled C_1 U-Pb age) and an $^{40}\text{Ar}/^{36}\text{Ar}$ intercept within error of the atmospheric ratio, suggesting the sample has not been significantly affected by either excess argon or argon loss. The apparent ages for the individual steps on the step heat, in the higher temperature portion of release (steps 10–19 of 19) are between 84.5 and 87.7 Ma and a mean age of 86.26 ± 0.62 Ma, within error of the inverse isochron age, suggesting that this isochron age is a useful estimate of the age of this sample.

Petrographic Information

A Nikon Eclipse LV100NPOL polarizing microscope was used to view the thin sections.

Sample petrography. The host rock micrite is variably recrystallized to microsparite (Fig.S8). The C_1 fibro-prismatic calcite cements have grown syntaxially (Durney and Ramsay, 1973) from the walls of vugs and fracture surfaces. Crystals range from 0.1- 2mm in length and vary slightly in their length/width ratio. The crystals generally coarsen toward the center of the vugs and often have pronounced growth zones marked by variable amounts of bitumen inclusions (Fig. S9). Though some inclusions appear to have leaked, the bitumen inclusions form laterally extensive growth zones within the vein fills and were clearly trapped during calcite precipitation.

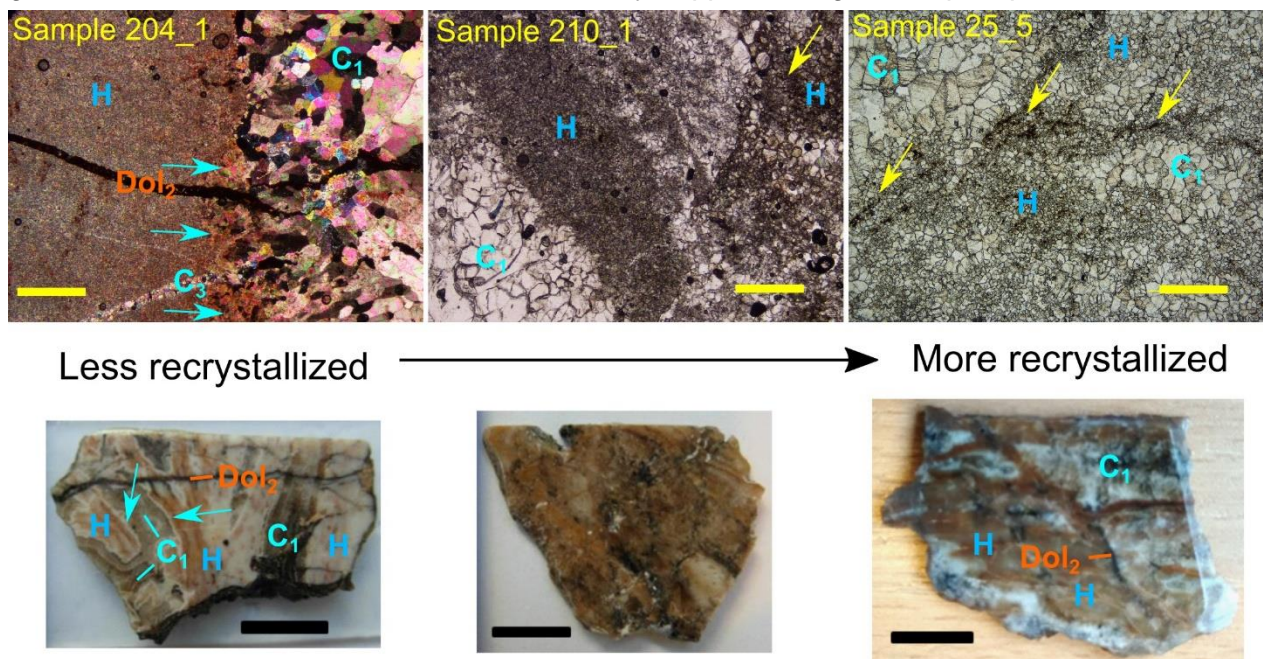


Figure S8, thin sections and corresponding polished blocks (below) showing trends in host rock (H) recrystallization and white/cream to brown coloration. Migrated intercrystalline bitumen has locally exploited dissolution/ recrystallization of the host rock (H) and contributed to the brown colouration. 204_1 is shown under cross-polarized light (XPL) and is stained with alizarin red. 210_1 and 25_5 are shown under plane polarized light (PPL). C_3 and Dol_2 cements are also highlighted. Pale blue arrows in the thin section image highlight areas of recrystallization along the walls of C_1 veins. Yellow arrows highlight intercrystalline bitumen that has infiltrated recrystallized H. Yellow scalebars= 0.5mm, black scalebars = 1cm.

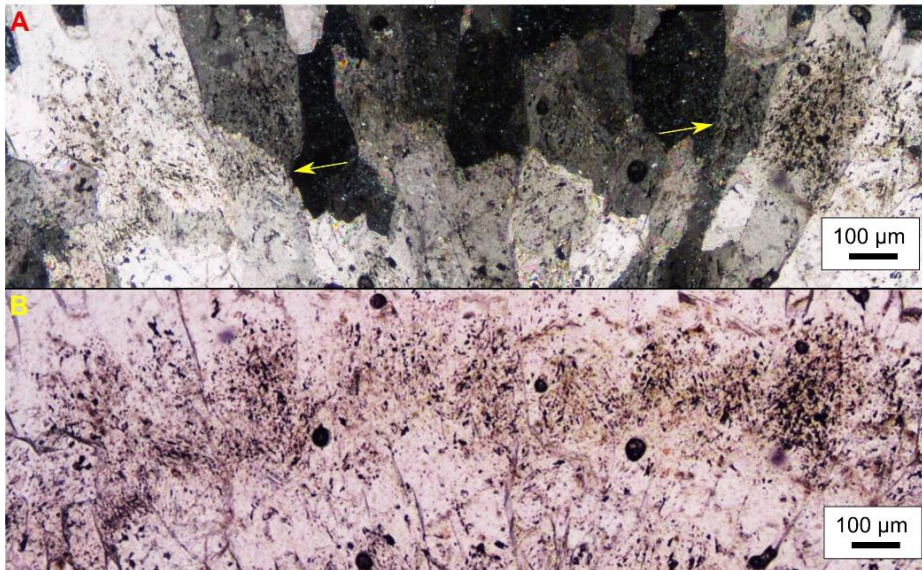


Figure S9, Detail of the bitumen-inclusion-rich band in Fig. 2. Note how inclusion trails reflect crystal growth banding (highlighted by yellow arrows). Large circular blobs are bubbles from thin section preparation. (A=XPL, B=PPL).

Minor dissolution and recrystallization of C_1 calcite to blocky sparite (C_2) crystals (<300 μm in size) and non-planar dolomite (Dol_1) crystals (<100 μm in size) has occurred locally. Bitumen sometimes occurs as an intercrystalline coating in association with C_2 and Dol_1 (Fig. 3, Fig. S10A) probably due to local remobilization from C_1 inclusions during recrystallization.

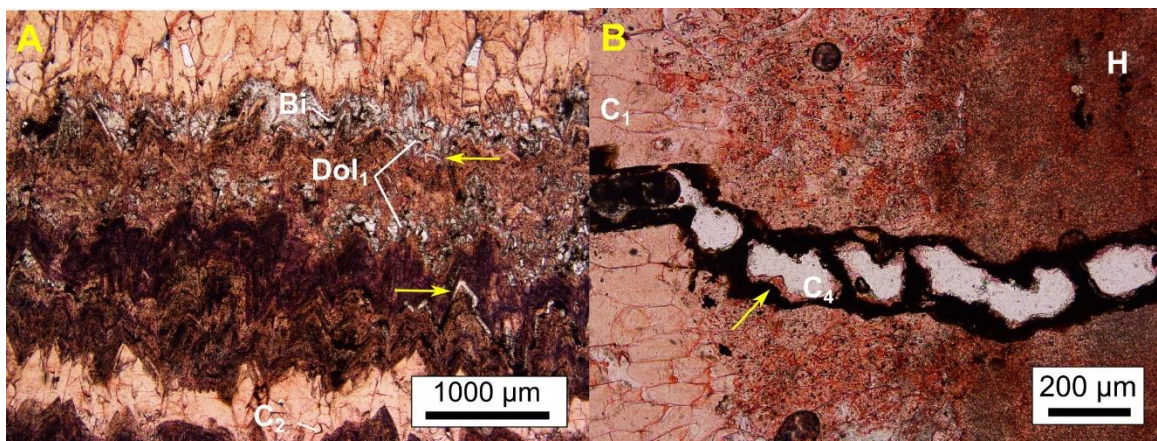


Figure S10, **A**, C_1 cement that has undergone relatively intense diagenetic alteration (stained with alizarin; PPL). Note the presence of both fabric destructive (non-planar) and somewhat fabric preserving (yellow arrows) Dol_1 dolomite. Bitumen sits between the dolomite crystals, rather than forming inclusions. A thin purple (Fe-rich) horizon runs through the center of the image (above the lower arrow), while C_2 recrystallization and dissolution are more visible in the limpid areas. **B**, calcite meniscus cements (C_4) growing on bitumen within a fracture (well-developed C_4 crystals indicated by yellow arrow) (white arrow = way-up; stained with alizarin red; PPL)

The above paragenetic sequence is cross-cut by partially cemented fractures. The first fracture fill is a fine dogtooth to blocky sparitic calcite cement (C_3). Fringing C_3 cements are present locally around a younger generation of dolomite filled (Dol_2) fractures, which always contain bitumen. The Dol_2 dolomite crystals are up to approximately 250 μm in diameter and generally coarsen toward the center of the veins. Some fractures are only partly filled by bitumen, but the uncemented, bituminous fractures can often be traced into sections that are cemented by Dol_2 . A

very fine (<50 μm), blocky fringing calcite cement (C_4) is the youngest phase identified. It nucleates on meniscus fabrics in the bitumen (Fig. S10B).

Carbon and Oxygen Stable Isotopic Data

Powdered samples of host rock and thick C_1 cements were acquired using a tungsten-tipped microdrill and were subsequently ground using a pestle and mortar. Stable isotope analysis was performed at the University of Liverpool using an automated on-line-system attached to a ThermoElemental Delta Plus XL mass spectrometer. Samples were reacted with phosphoric acid at 25°C for 30 minutes, and oxygen isotope ratios were corrected using a temperature-dependant isotopic fractionation factor (Friedman and O'Neil, 1989). Results are expressed in the standard delta notation as per mil differences to the V-PDB standard (‰VPDB). Estimated analytical precision (1σ), based on replicate analysis of laboratory calcite and dolomite quality control materials, is better than ± 0.1 ‰ for both carbon and oxygen delta values.

The measured $\delta^{18}\text{O}_{\text{calcite}}$ values (Table S1) were used to produce precipitation temperature estimates for C_1 cements (Fig. S11). Given that the cements formed during Upper Cretaceous greenhouse conditions (O'Brien et al., 2017; O'Connor et al., 2019) at a latitude of roughly 25°S (Torsvik et al., 2009), a conservative ambient surface temperature estimate of 25°C seems reasonable. Using typical meteoric water ($\delta^{18}\text{O}_{\text{water}}$) values of -2 to -20 (Standard Mean Ocean Water, SMOW; Moore and Wade, 2013), the C_1 cements could have precipitated from meteoric waters at ambient temperatures to around 40°C. The measured $\delta^{18}\text{O}_{\text{calcite}}$ values are equally compatible with precipitation from isotopically heavy (up to 10 ‰ SMOW) fluids at up to around 140°C (Fig. S11). The $\delta^{18}\text{O}_{\text{water}}$ for formation fluids can vary greatly with their salinity (Moore and Wade, 2013). Sheppard (1986) showed that the $\delta^{18}\text{O}_{\text{water}}$ values of primary magmatic waters are generally very positive and can reach around 10 ‰ (SMOW). Similar isotopic compositions would be expected for formation fluids that equilibrate with an active/very recent magmatic system (Sheppard, 1986; Taran et al., 1995).

Sample	Comments	$10^3 \delta^{13}\text{C}_{\text{VPDB}}$	$10^3 \delta^{18}\text{O}_{\text{VPDB}}$
25.3A	C1 vein outer rim	-9.71	-7.14
25.3B	C1 vein organic rich	-9.76	-6.99
25.3C	C1 vein	-10.28	-7.28
25.3D	host rock	-10.41	-6.32
25.5A	C1 vein organic rich	-10.07	-5.43
25.5B	host rock	-9.14	-6.45
204.1A	C1 vein	-19.90	-6.05
204.1B	host rock	-18.75	-5.58
208.2A	C1 vein	-11.00	-6.55
210.1A	C1 vein organic rich	-11.86	-7.23
210.1B	C1 vein	-6.40	-7.49

Table S2, summary of C and O stable isotope results.

A high C_1 precipitation temperature could add weight to the argument that kerogen was forcibly matured in the Late Cretaceous and was entrained by hot magmatic fluid (or magmatic-equilibrated fluid) before precipitating C_1 . A moderately ^{18}O -enriched fluid with a $\delta^{18}\text{O}_{\text{water}}$ of approximately 3 ‰ (SMOW) would have precipitated the C_1 calcite at around 70°C (Fig. S11), well within the oil window (> approximately 60°C; Schobert, 2013). However, it is also possible

that these fluids subsequently cooled, and/or mixed with meteoric water (which would have had to travel laterally beneath the impermeable evaporite prior to C₁ calcite precipitation).

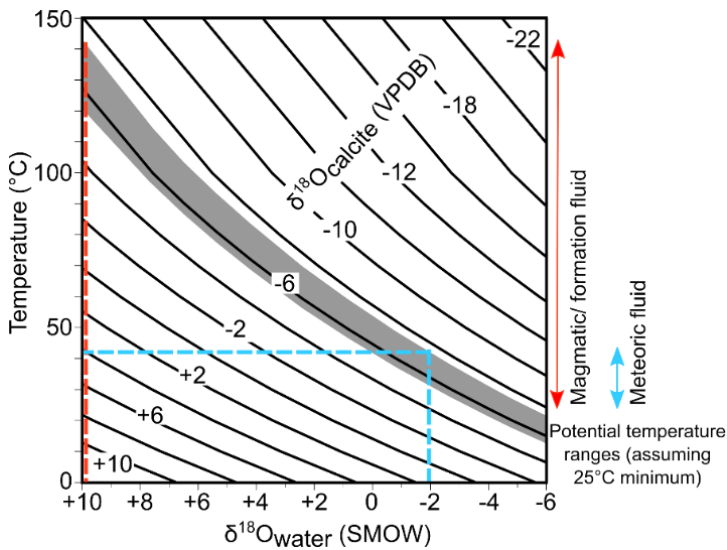


Figure S11, Equilibrium relationship between $\delta^{18}\text{O}_{\text{calcite}}$ (VPDB; curved lines), temperature and $\delta^{18}\text{O}_{\text{water}}$. Grey area = the range of measured $\delta^{18}\text{O}_{\text{calcite}}$ values for C₁ cements. Red dashed line = range of possible precipitation temperatures for magmatic/formation fluids ($\delta^{18}\text{O}_{\text{water}}$ not defined). Blue dashed line = temperature range for meteoric ($\delta^{18}\text{O}_{\text{water}}$ -2 to -20, Moore and Wade, 2013) fluids. Curved lines are from the calculation in Craig, (1965), the table is modified after Moore and Wade, (2013). Temperature

range estimates (double headed arrows) have an arbitrary lower cut-off of 25°C.

Major and Trace Element Data

Major and trace element analysis was conducted by the Manchester Analytical Geochemistry Unit using an Agilent 7500cx Inductively Coupled Plasma Mass Spectrometer (Th, U) and Perkin-Elmer 5300DV Inductively Coupled Plasma Atomic Emission Spectrometer (Fe, Ca, Sr, Mg, Mn, Si). Accuracy and precision were determined from repeat runs of standards (at concentrations from 0.05-10 ppb). Accuracy was better than 9%, except Mg (better than 15%) and Ca (better than 11%). Precision was better than 6% 1 σ RSD, except for Ca (better than 17% 1 σ RSD). Precision during sample runs was better than 5% 1 σ RSD, except for Th (better than 7% 1 σ RSD).

As stated above, the host rock has been partly recrystallised by vein fluids. Host rock trace element data reflect this, as there is not a great distinction between host rock and C₁ vein fills in terms of major/trace elements. Vein samples are generally richer in Sr and Mn (Table S2).

Sample	Phase	Concentration (ppm)							
		Fe	Ca	Sr	Mg	Mn	Si	Th	U
25.3A	C1 vein	109.19	298197.90	306.36	1583.75	8172.09	526.86	0.05	0.35
25.3B	C1 vein	948.76	289789.70	323.52	4805.74	10889.48	147.99	ND	1.55
25.3C	C1 vein	67.50	296464.30	286.07	1106.79	7630.71	287.14	ND	0.26
25.3D	host rock	802.39	331074.60	166.57	983.28	2523.58	240.90	0.05	0.27
25.5A	C1 vein	1289.39	315518.50	243.15	10669.85	7280.10	154.47	0.03	0.46
25.5B	host rock	1024.95	327030.90	156.49	1003.30	2106.80	247.42	0.09	0.30
204.1A	host rock	360.20	308296.80	231.70	1176.73	4068.47	161.89	0.02	0.07
204.1B	C1 vein	41.23	304665.50	247.38	1735.99	6856.06	143.22	ND	0.25
208.2A	C1 vein	401.32	293092.10	300.00	3009.21	7657.90	289.47	0.02	7.58
210.1A	C1 vein	315.33	304160.60	267.15	1796.72	7019.34	823.36	0.12	0.27
210.1B	C1 vein	448.36	320836.40	360.00	1705.09	4782.55	848.73	0.05	0.26

Table S2, summary of ICP-AES and ICP-MS Major and Trace Element Results. ND: below detection limit.

Bitumen Characterization and Interpretation

Characterization. The C₁ inclusions and Dol₂-associated (intercrystalline) bitumen in polished blocks were analysed using optical (including UV) microscopy (see above), Raman microscopy (Horiba XploRA PLUS Raman microscope) and Fourier Transform Infrared Microscopy (Perkin Elmer Spotlight 400 FT-IR). For Pyrolysis Gas Chromatography Mass Spectrometry (py-GC-MS), approximately 1 mg of each of the bituminous carbonate phases (C₁ and Dol₂) was extracted from sawn slices of a single sample (sample 204) using a scalpel. The bituminous powders were analysed by pyrolysis GC-MS (an Agilent 7890A/5975C GC/MSD system interfaced to a CDS-5200 pyroprobe). The pyroprobe was set at 300°C for 1 second, heated to 600°C at a rate of 20°C per millisecond at which it was held for 20 seconds. The interface was set at 300°C, the transfer line at 350°C and the valve oven at 325°C. Samples were analysed at a split ratio 20:1. For more details of the protocol, see Sparkes et al. (2016).

Results. None of the methods used were able to distinguish between the two bitumen phases. No detectable differences in reflectivity or fluorescence were identified from reflected light microscopy on the polished blocks. It was not possible to distinguish the phases based on their Raman or FTIR spectra. Pyrograms for both C₁- and Dol₂-associated bitumen were indistinguishable. The corresponding small peaks in both the C₁ and Dol₂ samples cannot be interpreted with confidence, because bitumen was not present in high enough concentrations to yield reliable results. The concentrated bitumen samples were all sticky and fairly viscous. The C₁ and Dol₂ bitumens appear to be geochemically similar, if not the same. The results suggest that either the C₁ bitumen was re-mobilized in the Dol₂ veins, or that the two bitumen phases were generated from the same or similar source rocks. Dol₂ dolomite is always associated with bitumen, whereas bitumen is conspicuously absent in the earlier vertical fracture generation (C₃; e.g., Figs 2-3), suggesting that the latter is the more likely scenario.

Interpretation. Several onshore bitumen seeps occur along the Angolan margin. Some Post-Salt seeps were sourced by Pre-Salt kerogen via local removal of the impermeable Aptian evaporite (e.g., Koning, 2014). However, it is often assumed that the kerogen matured via burial and migrated from the offshore basins (e.g., Koning, 2014). Late Cretaceous and Cenozoic igneous events (e.g., Jerram et al., 2018) have also influenced the development of petroleum systems in the South Atlantic. In Brazil, spatial associations between offshore oil fields and Eocene igneous trends suggest that the associated heat flow may have aided source rock maturation (Filho and Rodrigues, 1999; Filho et al., 2005). Offshore Angola, gas inclusions in U-Pb-dated Pre-Salt carbonates show that mantle-derived CO₂ has flushed otherwise productive reservoirs (e.g., Girard et al., 2017). Drilling campaigns in the offshore Kwanza Basin (Angola) have encountered several dry and/or heavily diagenetically-altered Pre-Salt carbonate reservoirs, raising questions about the effectiveness of the petroleum system on the African margin.

We have shown that forced maturation was likely responsible for the C₁ bitumen generation. The localized occurrence of C₁ in association with a volcanic center suggests that this occurred

within the onshore basin, rather than offshore. Overpressure fabrics imply that the ability of bituminous fluids to migrate within the Cangulo Fm. at the sample locality was limited in the Santonian. Thus, there could have once been a larger volume of stored hydrocarbons (at least locally) within the Pre-Salt succession. However, upon removal of the evaporite most the stored hydrocarbons (that were not bound within cements) are likely to have migrated into the overlying succession before being removed/degraded. The later (Dol₂-associated) residual bitumen is more likely to reflect the passage of hydrocarbons through the Cangulo Fm. in the Paleocene/Eocene (rather than storage), as the evaporite seal had likely been removed at the study locality.

REFERENCES

- Baqués, V., Moragas, M., Fabio, L., Zeller, M., Hunt, D., Casciello, E., Vergés, J., Cruz, I., Messenger, G., and Sharp, I., 2016, Diagenetic Evolution of the Cangulo Formation Pre-Salt Carbonates (Onshore Namibe Basin, Angola), *in* AAPG Annual Convention and Exhibition,.
- Beaudoin, N., Lacombe, O., Roberts, N.M.W., and Koehn, D., 2018, U-Pb dating of calcite veins reveals complex stress evolution and thrust sequence in the Bighorn Basin, Wyoming, USA: *Geology*, v. 46, p. 1015–1018, doi:10.1130/G45379.1.
- Beetz, P.F.W., 1933, Geology of South West Angola, between Cunene and Lunda Axis: *Transactions of the Geological Society of South Africa*, v. 36, p. 137–176, doi:10.1107/S0365110X6500422X.
- Coogan, L.A., Parrish, R.R., and Roberts, N.M.W., 2016, Early hydrothermal carbon uptake by the upper oceanic crust: Insight from in situ U-Pb dating: *Geology*, v. 44, p. 147–150.
- Craig, H., 1965, The measurement of oxygen isotope paleotemperatures.: Stable isotopes in oceanographic studies and paleotemperatures: *Consiglio Nazionale delle Ricerche*, p. 161–182.
- Durney, D.W., and Ramsay, J.G., 1973, Incremental strains measured by syntectonic crystal growths: *Gravity and tectonics*, p. 67–96.
- Hill, C.A., Polyak, V.J., Asmerom, Y., and P. Provencio, P., 2016, Constraints on a Late Cretaceous uplift, denudation, and incision of the Grand Canyon region, southwestern Colorado Plateau, USA, from U-Pb dating of lacustrine limestone: *Tectonics*, v. 35, p. 896–906, doi:10.1002/2016TC004166.
- Horstwood, M.S.A. et al., 2016, Community-Derived Standards for LA-ICP-MS U-(Th-)Pb Geochronology – Uncertainty Propagation, Age Interpretation and Data Reporting: *Geostandards and Geoanalytical Research*, v. 40, p. 311–332, doi:10.1111/j.1751-908X.2016.00379.x.
- Koning, T., 2014, Angola's oil industry—a century of progress in exploration and production, *in* American Association of Petroleum Geologists (AAPG) International Conference & Exhibition, p. 7–18.
- Lee, J.-Y., Marti, K., Severinghaus, J.P., Kawamura, K., Yoo, H.-S., Lee, J.B., and Kim, J.S., 2006, A redetermination of the isotopic abundances of atmospheric Ar: *Geochimica et Cosmochimica Acta*, v. 70, p. 4507–4512, doi:10.1016/j.gca.2006.06.1563.
- Li, Q., Parrish, R.R., Horstwood, M.S.A., and McArthur, J.M., 2014, U-Pb dating of cements in Mesozoic ammonites: *Chemical Geology*, v. 376, p. 76–83, doi:10.1016/j.chemgeo.2014.03.020.
- Ludwig, K., 2012, User's manual for Isoplot/Ex, Version 3.0. A geochronological toolkit for Microsoft Excel: *Berkeley Geochronol. Cent. Spec. Publ.* 5.,.
- Moore, C.H., and Wade, W.J., 2013, Carbonate reservoirs: Porosity and diagenesis in a sequence stratigraphic framework: *Newnes*, v. 67, 78–83 p.
- O'Brien, C.L. et al., 2017, Cretaceous sea-surface temperature evolution: Constraints from TEX86 and planktonic foraminiferal oxygen isotopes: *Earth-Science Reviews*, doi:10.1016/j.earscirev.2017.07.012.

- O'Connor, L.K., Robinson, S.A., Naafs, B.D.A., Jenkyns, H.C., Henson, S., Clarke, M., and Pancost, R.D., 2019, Late Cretaceous Temperature Evolution of the Southern High Latitudes: A TEX86 Perspective: *Paleoceanography and Paleoclimatology*, doi:10.1029/2018PA003546.
- Renne, P.R., Balco, G., Ludwig, K.R., Mundil, R., and Min, K., 2011, Response to the comment by WH Schwarz et al. on "Joint determination of 40K decay constants and 40Ar*/40K for the Fish Canyon sanidine standard, and improved accuracy for 40Ar/39Ar geochronology" by PR Renne et al.(2010): *Geochimica et Cosmochimica Acta*, v. 75, p. 5097–5100, doi:10.1016/j.gca.2011.06.021.
- Renne, P.R., Mundil, R., Balco, G., Min, K., and Ludwig, K.R., 2010, Joint determination of 40K decay constants and 40Ar*/40K for the Fish Canyon sanidine standard, and improved accuracy for 40Ar/39Ar geochronology: *Geochimica et Cosmochimica Acta*, v. 74, p. 5349–5367, doi:10.1016/j.gca.2010.06.017.
- Roberts, N.M.W., Rasbury, E.T., Parrish, R.R., Smith, C.J., Horstwood, M.S.A., and Condon, D.J., 2017, A calcite reference material for LA-ICP-MS U-Pb geochronology: *Geochemistry, Geophysics, Geosystems*, v. 18, p. 2807–2814, doi:10.1002/2016GC006784.
- Roberts, N.M.W., and Walker, R.J., 2016, U-Pb geochronology of calcite-mineralized faults: Absolute timing of rift-related fault events on the northeast Atlantic margin: *Geology*, v. 44, p. 531–534, doi:10.1130/G37868.1.
- Schobert, H., 2013, *Chemistry of fossil fuels and biofuels*: Cambridge University Press, 115 p.
- Sheppard, S.M.F., 1986, Characterization and isotope variations in natural waters: *Rev. Miner.*, v. 16, p. 165–183.
- Sparkes, R.B., Selver, A.D., Gustafsson, O., Semiletov, I.P., Haghypour, N., Wacker, L., Eglinton, T.I., and Talbot, H.M., 2016, Macromolecular composition of terrestrial and marine organic matter in sediments across the East Siberian Arctic Shelf:
- Spencer, C.J., Roberts, N.M.W., Cawood, P.A., Hawkesworth, C.J., Prave, A.R., Antonini, A.S.M., and Horstwood, M.S.A., 2014, Intermontane basins and bimodal volcanism at the onset of the Sveconorwegian Orogeny, southern Norway: *Precambrian Research*, v. 252, p. 107–118, doi:10.1016/j.precamres.2014.07.008.
- Taran, Y.A., Hedenquist, J.W., Korzhinsky, M.A., Tkachenko, S.I., and Shmulovich, K.I., 1995, *Geochemistry of magmatic gases from Kudryavy volcano, Iturup, Kuril Islands*: *Geochimica et Cosmochimica Acta*, v. 59, p. 1749–1761.
- Torsvik, T.H., Rouse, S., Labails, C., and Smethurst, M.A., 2009, A new scheme for the opening of the South Atlantic Ocean and the dissection of an Aptian salt basin: *Geophysical Journal International*, v. 177, p. 1315–1333, doi:10.1111/j.1365-246X.2009.04137.x.
- Woodhead, J.D., and Hergt, J.M., 2007, Strontium, Neodymium and Lead Isotope Analyses of NIST Glass Certified Reference Materials: SRM 610, 612, 614: *Geostandards and Geoanalytical Research*, doi:10.1111/j.1751-908x.2001.tb00601.x.